ACS OMEGA

Open Access



http://pubs.acs.org/journal/acsodf

Article

# Synthesis and Characterization of a Novel All-in-One Graphene Oxide-Nafion Polymer Bioconjugate for Application in Electrochemical Biosensing of the *Opisthorchis viverrini* Antigen

Nang Noon Shean Aye, Pornsuda Maraming, Patcharaporn Tippayawat, Sakda Daduang, Anchalee Techasen, Paiboon Sithithaworn, Roengrut Rujanakraikarn, Nichada Jearanaikoon, Rungrueang Phatthanakun, Ratchadaporn Supruangnet, Pat Photongkam, and Jureerut Daduang*

Cite This: *ACS Omega* 2025, 10, 13621−13633

Read Online

ACCESS | Metrics & More | Article Recommendations | Supporting Information

**ABSTRACT:** Bioconjugates in electrochemical biosensors can significantly enhance the detection process and sensitivity. In this study, we synthesized a monoclonal antibody-conjugated nanocomposite of graphene oxide and Nafion (GO-Nf-mAb) for application in an electrochemical biosensor as a novel all-in-one bioreceptor. The incorporation of Nafion (Nf) improved the stability, dispersity, and antibody immobilization on the GO surface, thereby increasing the sensitivity of the biosensor. The impact of Nafion on GO stability and antibody conjugation was thoroughly investigated and compared to that of Nafion-free conjugation via various characterization techniques, including X-ray photoelectron spectroscopy (XPS) and synchrotron radiation near-edge X-ray absorption fine structure. The presence of Nafion during monoclonal antibody (mAb) conjugation resulted in an increased peak intensity of the $NH_2$ band in XPS analysis and the highest intensity of C═O groups in O−K edge analysis, indicating a greater yield of the antibody. This innovative electrochemical biosensor exhibited a low detection limit of 1.68 ng $mL^{-1}$ in spiked urine, a wide linear range, and high reproducibility, outperforming conventional detection methods for *Opisthorchis viverrini* (OV) antigen detection. Our developed electrochemical biosensor introduces a novel and straightforward fabrication process using an all-in-one bioconjugate that serves as a bioreceptor, transducer, and blocking reagent simultaneously. Overall, this study offers a new insight on Nafion application in bioconjugation, and the GO-Nf-mAb conjugate-based electrochemical biosensor promises high sensitivity and a hassle-free immobilization process for OV antigen quantification.

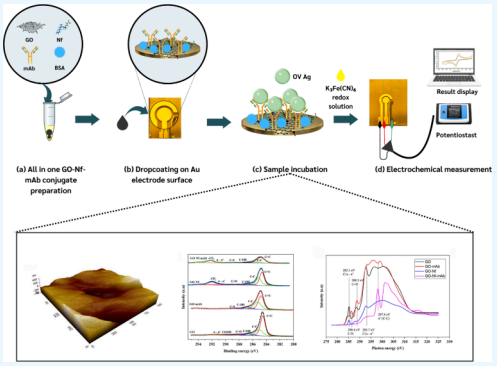


## 1. INTRODUCTION

Electrochemical biosensors for diagnosis and disease monitoring have been tremendously popular in recent decades because they offer several benefits such as simplicity, high sensitivity, selectivity, reproducibility, and low cost. The fabrication process, especially the immobilization of the bioreceptor and signal transduction, plays a major role in enhancing the sensitivity and specificity of the biosensor.[1] In fact, the selection of bioconjugation methods, immobilization procedures, and understanding of bioconjugate coupling chemistry on nanomaterial surfaces may strongly impact the development of novel and commercially viable biosensors.[2]

The application of bioconjugates in electrochemical biosensors can accelerate the detection process and increase the sensitivity. The fundamental step in the synthesis of an effective bioconjugate is the proper selection of cross-linking molecules that contain adequate reactive functional groups, which are required to couple with the other molecules, by using the chemical functionality available on the molecules.[3] Among the different conjugation methods, the most commonly used are adsorption, cross-linking with functional chemical reagents, covalent/noncovalent interactions, affinity interactions, and copolymerization within a polymeric matrix.[4]

An oxidized form of graphene, graphene oxide (GO), has been used for biomedical applications ranging from biosensor development to drug delivery for the treatment of diseases because of its dispersity in aqueous media and ability to provide a large surface area.[5] The presence of oxygen-containing functional groups in GO allows functionalization to support biorecognition in biosensor fabrication. In addition, electron transfer occurs at the edges and defects present in the structure of GO; hence, GO has become a promising material for electrochemical biosensing.[6] However, the self-aggregation

Received: January 21, 2025
Revised: February 19, 2025
Accepted: March 18, 2025
Published: March 28, 2025

of GO and the low yield of the GO-monoclonal antibody conjugate limited the sensitivity of the immunosensor.

Nafion is a perfluorinated sulfonate-based negatively charged copolymer that has been widely used for sensor modification because of its antifouling capacity, high permeability to cations, and chemical inertness. Moreover, the perfluoroalkyl backbones make Nafion hydrophobic, leading to an effective matrix to disperse carbon-based nanomaterials such as graphene and carbon nanotubes.[7−9] Furthermore, Nafion can enhance the stability of graphene oxide dispersions and the adsorption of electroactive molecules to electrode surfaces,[10,11] acts as a natural barrier against negatively charged particle interactions, and is commonly used for prevention of graphene aggregation.[12] When GO and the Nafion polymer were coupled and reduced into a functionalized nanocomposite, it offered good mechanical strength and enhanced conductivity comparable to pure graphene with improved biocompatibility. Additionally, this modification improves graphene's low capacitance by combining it with other conducting polymers, which raises graphene's conductivity and electrochemical efficiency.[13] Among the versatile applications, its use as an immobilization matrix of bioreceptors for the development of biosensors is certainly the most pervasive. In fact, there are countless examples of how Nafion is used to immobilize DNA-based, enzymatic, and antibody-based receptor probes.[1,14−16]

In this study, graphene oxide−Nafion polymer bioconjugates were synthesized for potential electrochemical detection of the OV antigen. Opisthorchiasis caused by the liver fluke (OV) is a neglected helminthic disease of public health significance.[17−20] Moreover, it is the most critical risk factor associated with cholangiocarcinoma (CCA) and is classified as a group 1 biological carcinogen. Early detection, diagnosis, and prevention of OV infection are an effective approach for addressing the high prevalence and control of the disease in endemic areas. So far, there is only a GO-mAb conjugate-based electrochemical biosensor for the OV antigen that has been developed by our group.[21]

To overcome the challenges of GO self-aggregation and lower antibody immobilization on the GO surface from our previous study, Nafion was applied as an ionic copolymer to enhance the conjugation process. Despite the common application of Nafion as an immobilization matrix for bioreceptors on electrodes being reported, the potential role of Nafion for bioconjugation has yet to be explored. Our study explicitly describes the properties of the GO-mAb conjugate with or without Nafion, in terms of functional, structural, and electrochemical aspects. The GO-Nf nanocomposites with high electroconductivity and active surface area served as transducing nanomaterials, which further support the antibody immobilization. Moreover, the bioconjugates were blocked with BSA before coating on electrodes, which can accelerate the biosensor fabrication process by dismissing the time-consuming, multistep procedures. The developed GO-Nf-mAb-based electrochemical biosensor exhibited high sensitivity, broad linearity, and great reproducibility.

## 2. RESULTS AND DISCUSSION

**2.1. Synthesis of the GO-Nf and GO-Nf-mAb Conjugates.** The conjugation of GO and Nafion occurred via physical adsorption, where the monoclonal antibody was conjugated via covalent interactions between the amine groups on the antibody and the carboxyl groups on the functionalized GO. Dynamic light scattering (DLS) measurements reflect the hydrodynamic diameter of the bioconjugate. The polydispersity index (PDI) and DLS size of GO, GO-mAb, GO-Nf, and GO-Nf-mAb were compared to understand the impact of Nafion on conjugation (Table 1). The presence of Nf certainly

**Table 1. Mean Hydrodynamic Diameter (*Z*-Average) and PDI of Different GO-mAb Conjugates**

| sample | *Z*-average (nm) | PDI |
|---|---|---|
| GO | 1297 ± 41 | 0.44 ± 0.04 |
| GO-mAb | 1895 ± 187 | 0.74 ± 0.12 |
| GO-Nf | 1185 ± 92 | 0.42 ± 0.03 |
| GO-Nf-mAb | 1461 ± 128 | 0.64 ± 0.09 |

enhances the dispersion of GO in an aqueous solution, leading to monodisperse GO-Nf-mAb conjugates. Both the DLS size and PDI of GO-Nf-mAb were lower than those of GO-mAb, indicating that Nafion prevented the aggregation of GO upon mAb conjugation.

**2.2. Physical and Electrochemical Stability of the GO-Nf Nanocomposite.** Nafion can enhance the dispersity of GO and the adsorption of electroactive molecules to electrode surfaces.[10,11] It acts as a natural barrier against negatively charged particle interactions and is commonly used for the prevention of graphene aggregation.[12] Therefore, the stability of the GO suspensions with or without Nafion was tested both optically and electrochemically. GO tends to aggregate easily upon standing, and frequent sonication is needed before use. Both the GO and GO-Nf solutions were stored by standing for 1 week without resuspension, and obvious aggregates of GO were observed at the bottom with a clear supernatant after day 4. Moreover, GO-Nf aggregated more slowly than did GO and remained stable after day 7 (Figure S1a−g).

The cyclic voltammograms (CV) of GO and GO-Nf were performed daily to observe the changes in the anodic peak current ($I_{pa}$) signals. The peak current of GO-Nf was stable from day 1 (58.24 $\mu$A) to day 7 (59.22 $\mu$A). In contrast, that of the GO solution was turbulent and declined rapidly from 92.08 $\mu$A on day 1 to 84.6 $\mu$A on day 7 (Figure S1h). These results confirmed that the modification of GO with Nafion significantly improved the dispersity and stability of GO in aqueous solutions and on electrode surfaces. The electrochemical signal of GO-Nf is observed to be lower than that of GO. The ferri/ferrocyanide anions are negatively charged and were unable to diffuse through Nafion due to their size and charge, and hence, the electron transfer reaction was hindered. This can be attributed to the covering effect of the Nafion backbone, which prevents the fluoropolymer attractive properties of the electrochemical probe.[22,23] However, only 0.5% Nafion was applied in the conjugate, making sure that the anodic redox species were not fully blocked.

**2.3. Surface Characterization of the GO-Nf-mAb Nanoconjugate-Modified Immunosensor.** FE-SEM images of the E-beam-evaporated gold (Au) electrode revealed a uniform surface with small gold nanoparticles (Figure S3). The immobilization of GO and GO-Nf on the electrode surfaces resulted in a flake-like structure. The GO-Nf-mAb nanocomposite consists of several layers of GO covered with a weblike structure of the antibody, indicating the complete conjugation of the antibody on GO-Nf. The results of the FE-SEM and AFM topology were in agreement.

The 3D surface topologies of the fabricated Au working electrode and the modified sensor surface were acquired via



https://doi.org/10.1021/acsomega.5c00633
ACS Omega 2025, 10, 13621−13633

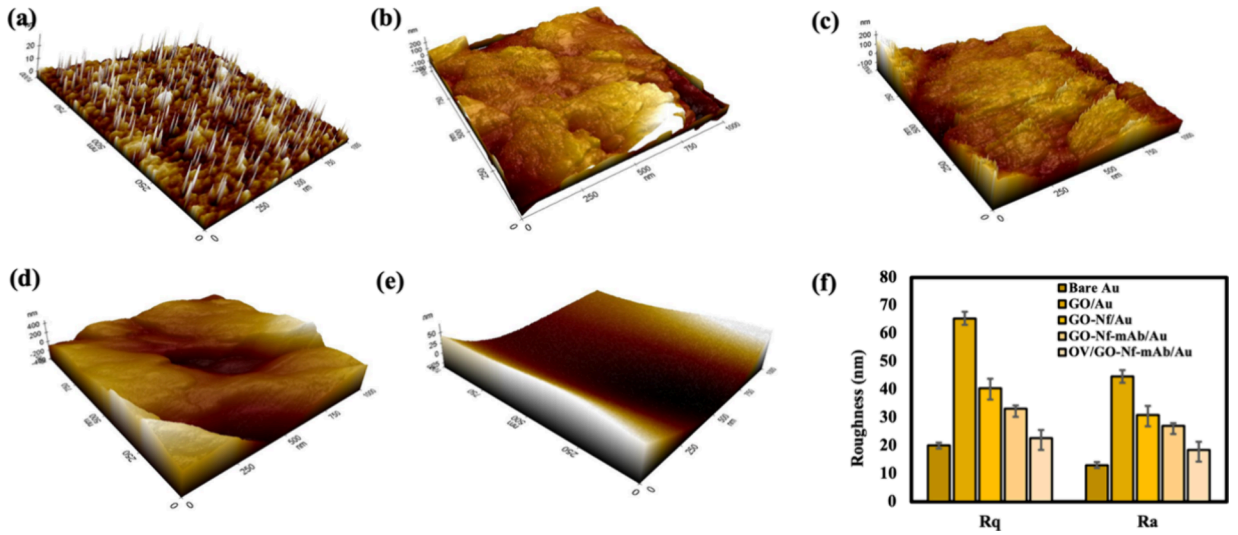


**Figure 1.** AFM images of the (a) bare Au electrode, (b) GO-modified Au electrode, (c) GO-Nf-modified Au electrode, (d) GO-Nf-mAb-modified Au electrode, and (e) OV Ag-immobilized GO-Nf-mAb/Au electrode; (f) root-mean-square ($R_q$) and average ($R_a$) surface roughness of each modification.

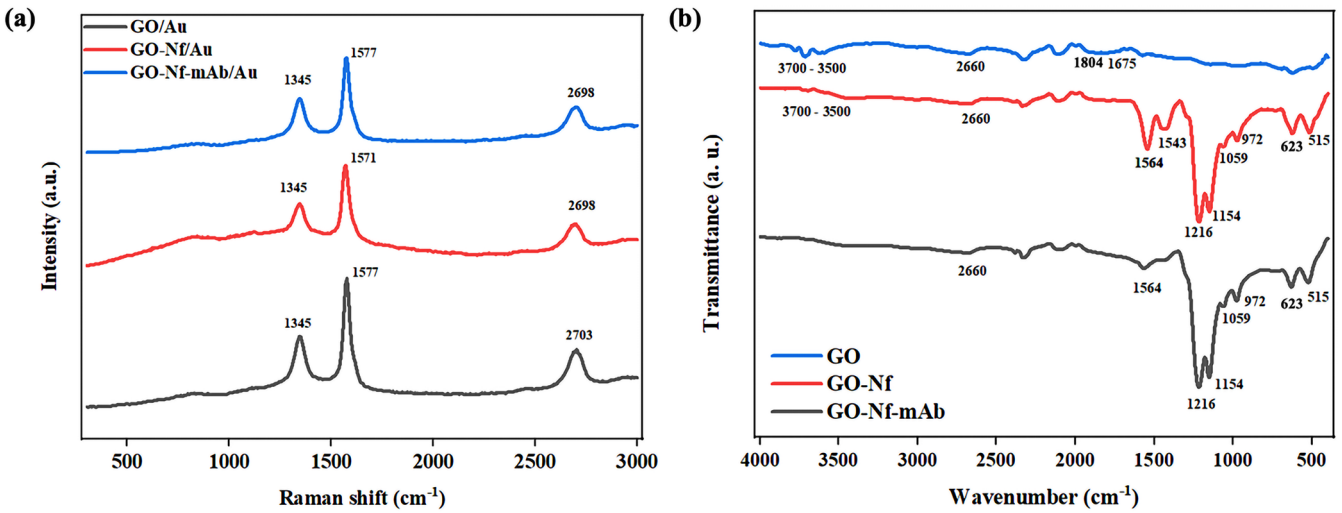


**Figure 2.** (a) Raman spectra and (b) ATR-FTIR spectra of the GO-modified Au electrode (blue), GO-Nf-modified Au electrode (red), and GO-Nf-mAb-modified Au electrode (black).

atomic force microscopy (AFM). The root-mean-square (RMS) surface roughness ($R_q$) and average surface roughness ($R_a$) were compared for different immobilization procedures (Figure 1). The bare electrode exhibited an $R_q$ of 20 ± 2.3 nm and an $R_a$ of 13 ± 3.04 nm (Figure 1a). The modification of the Au electrode with GO and the GO-Nf nanocomposite resulted in increases in the levels of $R_q$ and $R_a$. The $R_q$ and $R_a$ values of the GO-modified electrode were 65.4 ± 3.5 and 44.6 ± 3.5 nm, respectively (Figure 1b). In contrast, the GO-Nf-modified electrode exhibited smoother surfaces with $R_q$ and $R_a$ values of 40.5 ± 3.29 and 30.9 ± 3.29 nm, respectively (Figure 1c). Compared with GO modification, immobilization with the GO-Nf nanocomposite resulted in a smoother and more homogeneous morphology because of the complete dispersity of GO and the film-like structure of Nafion. Furthermore, the modification of the electrode surface with the GO-Nf-mAb nanoconjugate resulted in a lower surface roughness, with $R_q$ and $R_a$ values of 33.2 ± 1.1 and 27 ± 2.9 nm, respectively (Figure 1d). The binding of OV Ag on the sensor surface resulted in the lowest $R_q$ (22.6 ± 3 nm) and $R_a$ (18.4 ± 3 nm) values because the larger molecular structure of the OV antigen formed an additional layer on the electrode surface (Figure 1e). The RMS of GO-Nf-mAb was decreased compared to the GO-Nf-modified electrode due to the presence of an antibody on the rough surface of the GO-Nf nanocomposite, which agrees with the surface morphology by FE-SEM analysis. The RMS was further decreased after OV antigen binding because of the globular shapes of antigens, resulting in a smoother surface morphology. However, the RMS of the antibody and OV antigen immobilization were increased compared to that of the bare Au surface, indicating the surface immobilization procedure. Our findings are consistent with the previous report of Jain et al., mentioning that the presence of the antibody and BSA on the mesoporous carbon-modified surface induced the RMS reduction.[24] Other studies (Ohno et al. and Törer et al.) confirmed that the binding of protein on the antibody-coated surface resulted in a smoother morphology.[25,26]



https://doi.org/10.1021/acsomega.5c00633
ACS Omega 2025, 10, 13621−13633

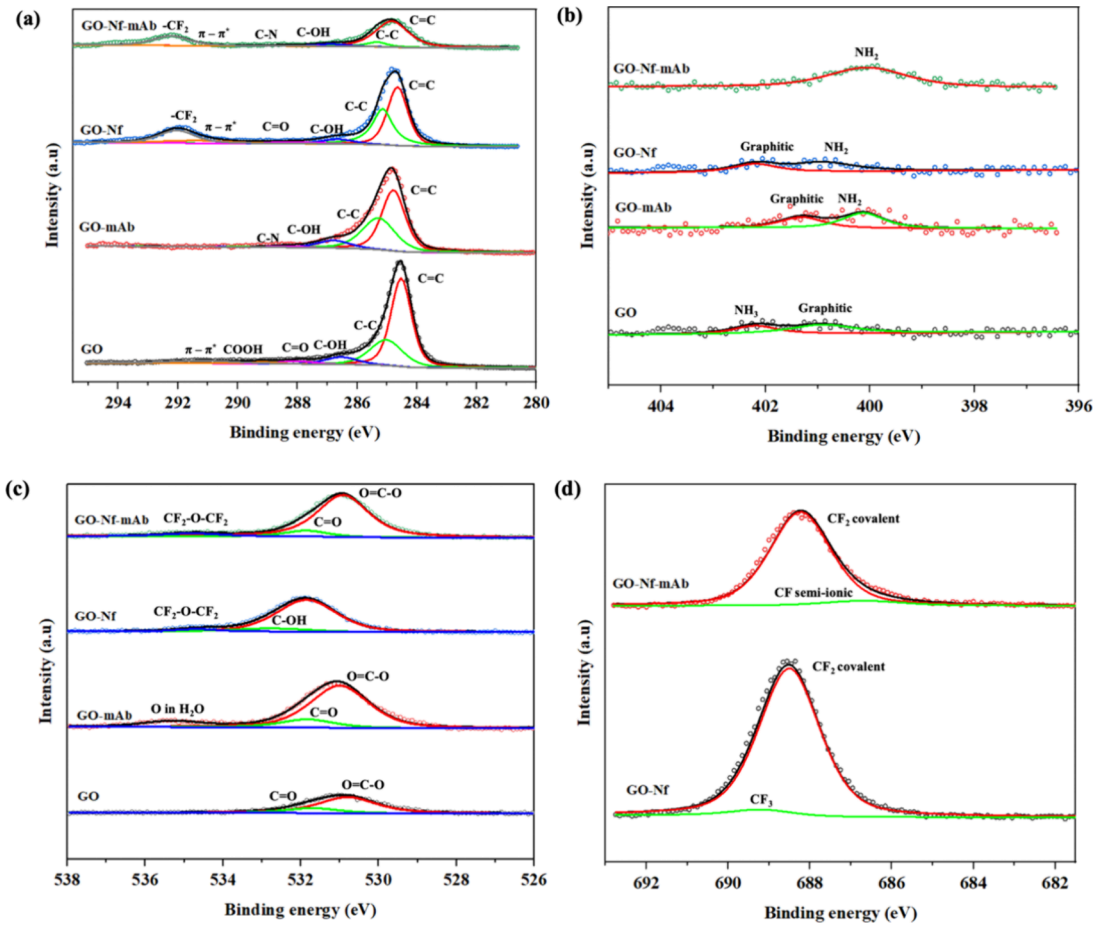


**Figure 3.** (a) C 1s, (b) N 1s, and (c) O 1s XPS spectra of GO, GO-mAb, GO-Nf, and GO-Nf-mAb; (d) F 1s XPS analysis of GO-Nf and GO-Nf-mAb.

The Raman spectra of GO, GO-Nf, and GO-Nf-mAb were dominated by D and G peaks, which are the prominent peaks in all of the graphene-like systems (Figure 2a). The Raman spectra of all three modified samples were observed at 1345 and ~1577 $cm^{-1}$, which corresponded to the D and G bands of graphene, respectively. Second-order Raman scattering of the 2D bands, a sensitive indicator of the number of graphene layers, was observed at approximately 2700 $cm^{-1}$. The D band is associated with breaking the $sp^2$ symmetry of carbon by structural disorder and defects due to the presence of heteroatoms and grain boundaries.[27] Furthermore, the G band represents the first-order scattering of the stretching vibration mode ($E_{2g}$) observed for $sp^2$ carbon domains.[28] The ratio of the integrated intensities of the D and G bands ($I_D/I_G$) is taken as an indicator of the relative disorder present in graphitic structures. The intensity ratio and $I_D/I_G$ ratio for GO/Au and GO-Nf/Au were 0.59 and 0.70, respectively, which indicated an increase in the amount of disordered $sp^3$ mode and depicted the attachment of Nf chains on GO.[29] Furthermore, the G band for GO-Nf/Au shifted toward a lower frequency of ~6 $cm^{-1}$with respect to that of GO/Au. A decrease in the $I_D/I_G$ ratio to 0.61 was observed for GO-Nf-mAb/Au. The decrease in the $I_D/I_G$ intensity was due to the aggregation of the mAb on the GO-Nf layer and the increase in the number of graphitic domains, which led to the second amorphization stage beyond the critical defect density.[30]

Attenuated total reflectance-Fourier transform infrared (ATR-FTIR) characterization was carried out for the functionalization of GO with Nafion and the antibody (Figure 2b). A C−H bending (aromatic) functional group was observed at 1804 $cm^{-1}$, and the peak at 1675 $cm^{-1}$ represented the C═O stretching carboxyl group of GO,[31] which later disappeared in GO-Nf and GO-Nf-mAb conjugates as the carboxyl group was taken up by the amine group of the monoclonal antibody. The band at 2660 $cm^{-1}$ was attributed to the O−H stretching of GO, GO-Nf, and GO-Nf-mAb. These factors contribute to the characteristics of GO, as reported in previous studies.[32−35] The appearance of characteristic peaks corresponding to the bending of the amide II band at 1543 and 1564 $cm^{-1}$ indicates the presence of the antibody structure on the GO-Nf surface. The hydroxyl groups with all C−OH variations from COOH and $H_2O$, which were observed between 3700 and 3500 $cm^{-1}$, disappeared upon antibody conjugation.

In the ATR-FTIR analysis of GO-Nf and GO-Nf-mAb, the asymmetric and symmetric stretches of the $-CF_2$ groups at 1154 and 1216 $cm^{-1}$, which are typical for Nafion, were observed.[29,36,37] Moreover, the GO-Nf and GO-Nf-mAb nanocomposites showed changes in the −COC− symmetric stretching bands at 972 $cm^{-1}$, the stretching band of the C−S group at 623 $cm^{-1}$, the symmetric O−S−O bending band at 515 $cm^{-1}$, and the $-SO_3-$ stretching vibration band at 1059 $cm^{-1}$. The broad band in the frequency region between 1460 and 1410 $cm^{-1}$ was derived from the bands of C−F groups in amorphous polytetrafluoroethylene.[38−41]


https://doi.org/10.1021/acsomega.5c00633
ACS Omega 2025, 10, 13621−13633

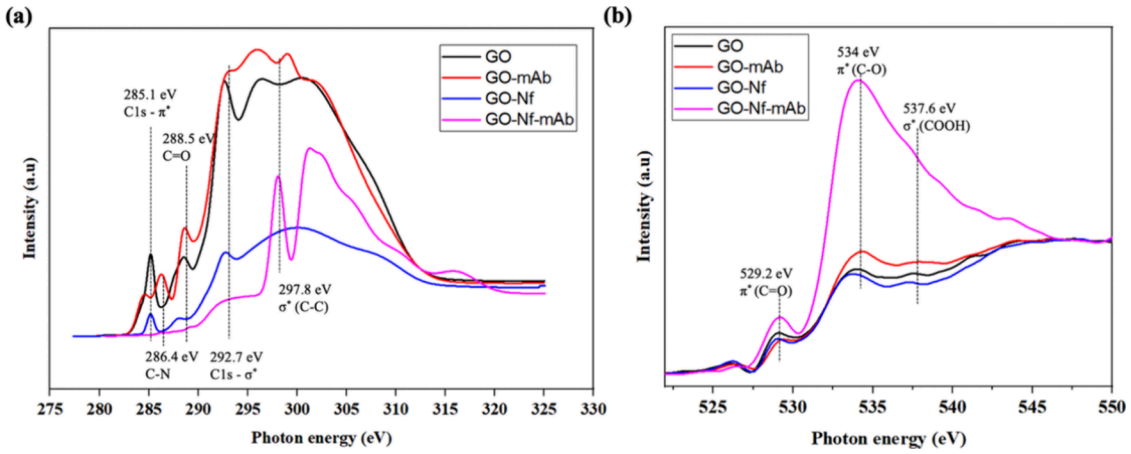


**Figure 4.** (a) C−K edge and (b) O−K edge NEXAFS spectra of GO, GO-mAb, GO-Nf, and GO-Nf-mAb.

**2.4. XPS Analysis.** The percentages of relative carbon, nitrogen, and oxygen in each sample are described in Table S2. Fluorine (F) atoms were exclusively detected in samples containing Nafion. The oxygen (O) content was the highest in the GO-Nf-mAb samples, whereas the nitrogen (N) percentage was the lowest. This phenomenon was probably because antibody conjugation on GO-Nf resulted in an increase in the number of carboxyl groups and a decrease in the number of graphitic N domains, which clearly confirmed the presence of pure $NH_2$ groups in the fine-scan N 1s analysis. The detailed characteristics of the XPS compositional analysis are explained in Table S3. Figure 3 shows the high-resolution C 1s, N 1s, O 1s, and F 1s spectra of GO and the mAb conjugates of GO with or without Nafion. The C 1s XPS spectra of all the samples were deconvoluted into three components at ∼284.53, 285.03, and 286.53 eV, representing C═C ($sp^2$), C−C, and C−OH, respectively, which are typical characteristics of GO (see Figure 3a).[42−44] The highest $sp^2$ content was found in GO without any modifications, as the addition of Nafion and the antibody resulted in defects in the $sp^2$ structure of GO. $\pi-\pi^*$ interactions were observed at ∼291.2 eV in the GO, GO-Nf, and GO-Nf-mAb samples as Nafion chains attached to the GO surface by physical adsorption. Moreover, $CF_2$ bonding was observed at 292.03 and 292.22 eV in the Nafion-containing samples, indicating the successful conjugation of Nafion on the GO surface. The immobilization of the antibody with GO was confirmed by the appearance of a C−N band at 288.29 eV in GO-mAb and 288.34 eV in GO-Nf-mAb. Amide bands were also observed in antibody-conjugated samples at ∼400 eV.[45−47] The presence of peak at 402 eV binding energy in the GO sample is attributed to photoemission from N−C═O due to the NHS ester group.[48] The presence of Nafion during antibody conjugation resulted in an increased peak intensity of the $NH_2$ band, indicating a greater yield of monoclonal antibodies (Figure 3b). In contrast to the lower nitrogen (N) percentage in the wide scan, the N1 s spectra were deconvoluted into a single $NH_2$ peak, indicating the presence of more amide bonds in the GO-Nf-mAb samples than in the other samples. The O1 s analysis revealed O−C═O and C═O peaks at ∼530.8 and 531.7 eV, respectively, in all the GO samples.[49,50] The additional peak at 534.8 eV indicated the formation of $CF_2$−O−$CF_2$ upon Nafion binding (Figure 3c). Compared with the unconjugated samples, the mAb-conjugated GO and GO-Nf samples presented the highest oxygen contents. F 1s spectra were detected only for GO-Nf and GO-Nf-mAb (Figure 3d). The deconvoluted peak at ∼688.5 eV was attributed to the $CF_2$ covalent bond.[51] Overall, the binding of Nafion chains on GO surfaces was confirmed by the increased intensity of $\pi-\pi^*$ transitions, decreased $sp^2$ due to defects on GO, and the emergence of the $-CF_2$ band.[29,52,53] The presence of Nafion enhanced the antibody immobilization on the GO surface and stabilized the GO functionality. Furthermore, the $sp^2$ ratio from the XPS analysis aligns with the NEXAFS results and the $I_D/I_G$ ratio from the Raman measurements.

**2.5. Synchrotron Radiation Near-Edge X-ray Absorption Fine Structure (NEXAFS) Measurement.** NEXAFS provides information on the electronic structure, surface chemistry, and steric orientations of specific chemical bonds.[54] The carbon K edge and oxygen K edge absorption spectra of GO and GO-Nf before and after conjugation with the antibody are shown in Figure 4. The absorption edge at 285.1 eV corresponds to the transition from the C 1s core level in the $sp^2$ network into the $\pi^*$ band, and the resonance at 292.7 eV, which is related to the C 1s transition to dispersionless states of $\sigma^*$ symmetry, characterizes the distinct and strong angular dependency of GO.[54−56] The absorption intensities of these features were greater for GO than for the modified conjugates, as GO is expected to have more $sp^2$ hybridization. The covalent functionalization of GO with mAb resulted in a C−N band at 286.4 eV in C 1s XPS and C−K edge analysis. A decrease in $sp^2$-related transitions suggests significant disruption to the $\pi$-conjugated network, proportional to the extent of covalent modifications. As more antibody was conjugated to the GO surface, the increase in the nitrogen content led to nitrogen substitution in the graphite network. The emergence of C−N bonds in the antibody-containing samples indicated the successful conjugation of antibodies on the GO surface. These findings are similar to previously reported studies.[55,57,58] The O−K edge spectra revealed a C═O bond at 529.2 eV, and the $\pi^*$ band was the highest in the GO-Nf-mAb conjugate. NEXAFS complements XPS by confirming the presence of specific bonds and electronic transitions that occur near the GO surface. It further provides information on the structures of conjugates, specifically the $\pi^*$ band, which is more prominent in GO-Nf-mAb conjugation. This implies that new stable $\pi-\pi$ interactions or electron-rich functional groups have formed among the GO, Nafion, and antibody components, indicating a strong conjugation. Moreover, NEXAFS further reveals the insights on how conjugation


https://doi.org/10.1021/acsomega.5c00633
ACS Omega 2025, 10, 13621−13633

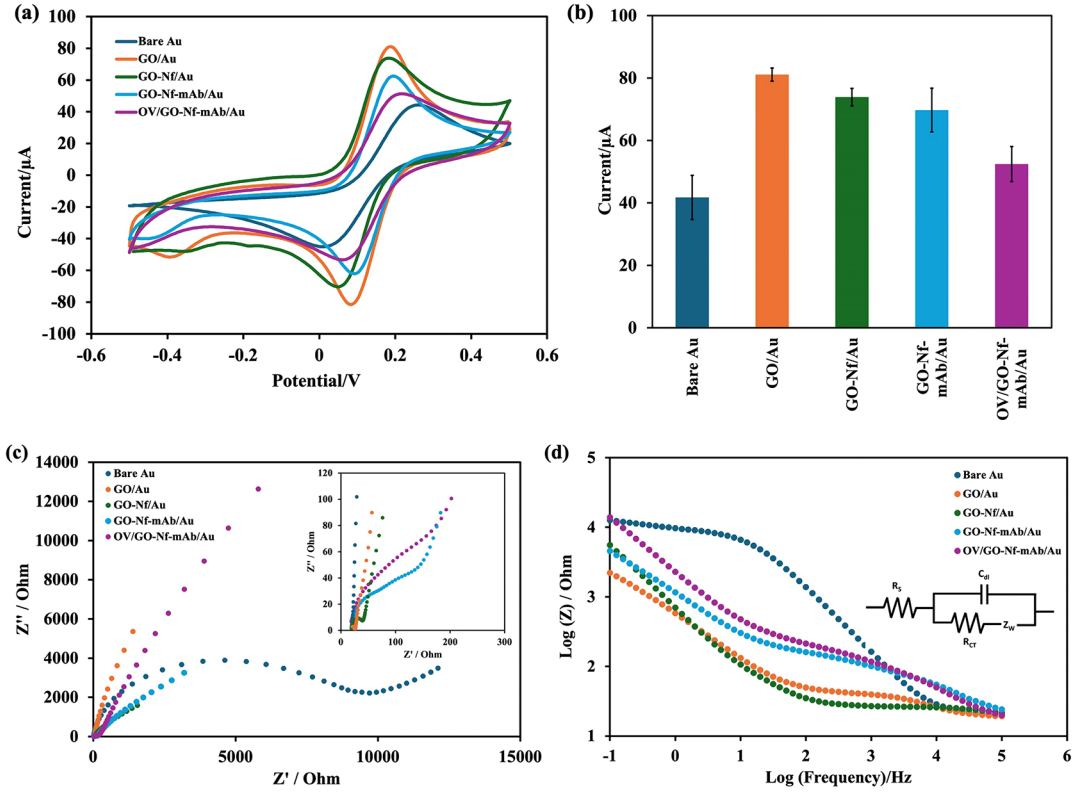


**Figure 5.** (a) Cyclic voltammograms and (b) anodic peak currents of different sensor modifications. Electrochemical impedance spectroscopy (EIS) measurement of the sensor: (c) Nyquist plot and (d) Bode plot showing the magnitude of impedance against frequency. The inset shows the Randles circuit for EIS fitting.

affects the anisotropic electronic properties of GO. The results of the XPS, NEXAFS, and Raman spectra confirm the successful conjugation of Nafion chains on the GO surface as well as the enhanced immobilization of the monoclonal antibody on the GO-Nf nanocomposite.

**2.6. Electrochemical Characterization of the Immunosensor.** The electrochemical behavior of the fabricated electrode interface was characterized by CV and electrochemical impedance spectroscopy (EIS) using a redox indicator (Figure 5). During CV, the fabricated immunosensor exhibited a typical cyclic voltammogram with anodic ($I_{pa}$) and cathodic ($I_{pc}$) peaks at approximately 0.2 mV (Figure 5a). The anodic peak current values after each modification procedures are depicted in Figure 5b. After modification of the Au electrode surface with GO, the peak current was observed to be increased from 41 $\mu$A in the bare electrode to 81 $\mu$A in the GO-modified electrode. This phenomenon is explained by the increased electroactive area and conductivity of GO immobilized on Au. Our finding aligns with the enhanced electrical behavior of GO in the electrochemical biosensor as reported in previous studies.[59−61] Although GO has lower conductivity than its reduced form due to the presence of oxygen-containing functional groups, the fine-tuning of oxidation parameters and the degree of oxidation to control structural defects can turn GO to be an insulator, semiconductor, or semimetallic material.[62] Although the results appear to contradict the conventional understanding of GO's insulating nature,[63] the enhanced conductivity can be attributed to several factors such as the GO structure, properties, and self-assembly of the GO monolayer on the Au electrode contributing to the enhanced electron transfer pathway. The currents were relatively decreased after immobilization of GO-Nf (74 $\mu$A) and GO-Nf-mAb (69 $\mu$A) due to the electrochemical hindering activity of anionic Nafion ions and negatively charged antibodies on the GO surface.[63,64] The peak current further decreased to 52 $\mu$A after target recognition because the specific binding of the monoclonal antibody and OV antigen complex acted as a kinetic barrier on the electrode surface, where the redox particles could not penetrate the layers into the conductive electrode surfaces. The electroactive areas of the sensor surface after stepwise immobilization were calculated in the presence of 5 mM $[Fe(CN)_6]^{3-/4-}$ by the Randles−Sevcik equation as follows:

$$I_p = 2.69 \times 10^5 A \times D^{1/2} n^{3/2} v^{1/2} C$$

where $I_p$ is the peak current of the electrode, $n$ is the number of electrons transferred in the reaction (here, $n$ = 1), $D$ is the diffusion coefficient ($7.26 \times 10^{-2}$ cm$^2$ s$^{-1}$), $A$ is the surface area of the electrode (the diameter is 0.3 cm, and the geometrical surface area is 0.07 cm$^2$), $C$ is the concentration of the electroactive redox chemical (here, $5 \times 10^{-6}$ mol cm$^{-3}$), and $v$ is the scan rate (100 mV s$^{-1}$). The effective surface area of the modified electrodes is directly proportional to the peak currents of the electrodes. In this study, the effective surface area of the bare electrode was 0.011 cm$^2$, which was later amplified to 0.022 cm$^2$ in GO/Au, indicating improved electroactivity. The decrease in the electroactive area, 0.02, 0.019, and 0.014 cm$^2$ after GO-Nf, GO-Nf-mAb, and OV antigen binding, respectively, was related to the hindering of electron transfer activity by the antigen−antibody reaction.

The Nyquist plot obtained for the bare electrode, GO/Au, GO-Nf/Au, and GO-Nf-mAb/Au is shown in Figure 5c. As


https://doi.org/10.1021/acsomega.5c00633
ACS Omega 2025, 10, 13621−13633

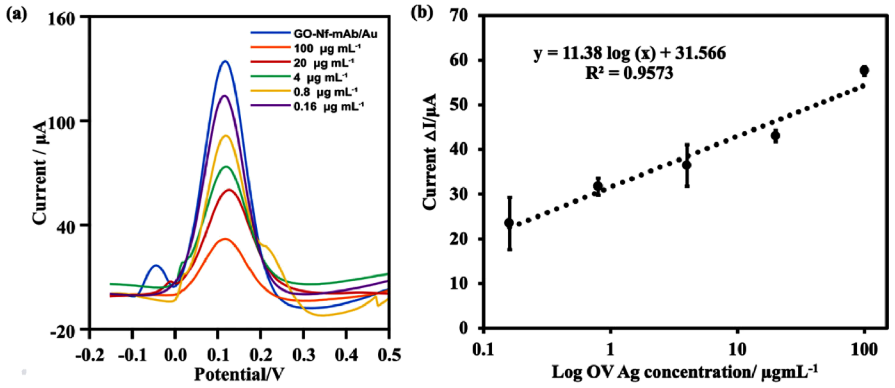


**Figure 6.** (a) DPV responses of the GO-Nf-mAb modified sensor (baseline) and different concentrations of OV spiked in urine and (b) standard curve of the immunosensor showing the linear relationship between the logarithm of OV Ag concentration (0.16−100 $\mu$g mL$^{-1}$) and corresponding maximum current ($\Delta I$) measured by DPV.

can be seen, a semicircle was observed at the high frequency region, and the diameter of this semicircle is equivalent to the charge-transfer resistance across the electrode interface. The qualitative analysis of the Nyquist plots showed the decrease in the semicircle diameter for the modified electrodes with GO, GO-Nf, and GO-Nf-mAb, indicating an improvement of the charge transfer in these electrodes compared to the unmodified Au electrode. A Randles equivalent circuit was fitted to the Nyquist plots to extract quantitative impedance data.

The Randles equivalent circuit models the electrochemical system using the following electrical components: the supporting electrolyte resistance ($R_s$) in series with the parallel combination of the double-layer capacitance ($C_{dl}$), charge-transfer resistance ($R_{ct}$), and a Warburg impedance ($Z_W$) (see the inset, Figure 5d). From this fitting, the following $R_{ct}$ values were obtained: 7689 Ω for bare Au, 0.2 Ω for GO/Au, 7.04 Ω for GO-Nf/Au, 49.9 Ω for GO-Nf-mAb/Au, and 52.9 Ω for OV/GO-Nf-mAb/Au. The dramatic decrease in charge-transfer resistance after modification indicates that the GO-based platform significantly enhances interfacial electron transfer, despite the presence of Nafion and antibodies. This phenomenon can be explained by several factors: (1) With GO's electronic properties, GO can exhibit semiconductor or semimetallic behavior depending on the oxidation parameters and structural defects.[62] In our case, the GO preparation method likely results in a material with enhanced conductivity. (2) For surface area effects, GO provides a significantly larger electroactive surface area compared to bare gold, potentially creating multiple electron transfer pathways that compensate for any insulating effects of the surface modifications, as supported by previous studies.[59−61] Importantly, a one-step GO-Nf-mAb bioconjugate modification was employed rather than sequential layer-by-layer deposition on the Au electrode. This approach minimizes the interfacial barriers and maintains efficient electron transfer. The EIS results correlate well with our CV measurements, confirming the enhanced electrochemical properties of the modified electrode surface.

Furthermore, the Bode plot of the modified sensor (Figure 5d) shows the magnitude of the impedance in relation to the frequency. The higher magnitude of the impedance at the lower frequency region indicates the higher resistance of the electrode. Hence, both Nyquist and Bode plots exhibit the decrease resistance of the GO-modified sensor, followed by increasing impedance with subsequent modification, which in turn agree with the CV measurement. The electrochemical characterization of the sensor confirms the successful immobilization of the GO-Nf-mAb conjugate and the detection of the OV antigen.

**2.7. Analytical Performance of the GO-Nf-mAb/Au Immunosensor.** Under optimal experimental conditions, the applicability of the developed immunosensor to detect OV antigens was examined. The differential pulse voltammogram (DPV) was recorded before the sensor surface was incubated with the target antigen, and the peak current was extracted as the baseline ($I_0$) signal. During the electrochemical measurement, the immobilized GO-Nf-mAb conjugate exhibited free and stable assembly on the electrode surface, indicating a significant peak current of the redox solution. As the concentration of the OV antigen bound to the immobilized antibody increased, the antigen−antibody complex acted as a hindrance on the electrode surface, and fewer redox species were able to penetrate it, leading to a reduction in relative signal (Figure 6a). For OV sensor calibration, the electrochemical signal of the GO-Nf-mAb/Au sensor was measured as a baseline ($I_0$) and the signal after OV antigen incubation was measured as $I_1$. The peak current changes ($\Delta I = I_0 - I_1$) were calculated to observe the correlation with the OV antigen concentration present in the sample.

OV antigen detection is commonly carried out in urine samples as a noninvasive sample collection. Even in the case of low-intensity infection and bile duct obstruction, the metabolic products can be secreted from adult worms and the OV antigen can readily be detected in urine. Moreover, urine OV antigens were reported to be significantly correlated with the intensity of OV infection.[65] To equilibrate the interference of other substances in urine on OV antigen detection, a standard curve was calibrated using serially diluted concentrations of the OV antigen (0.16−100 $\mu$g mL$^{-1}$) spiked into undiluted urine samples. As the concentration of the OV antigen in urine increased, a decrease in the DPV peak current was observed. Peak current changes increased linearly ($I$ = 11.38 log($c$) + 31.57) with an $R^2$ of 0.957 with respect to the OV antigen content (0.16−100 $\mu$g mL$^{-1}$) (see Figure 6b). The slight deviation observed at 20 $\mu$g mL$^{-1}$ may indicate the onset of surface saturation effects or kinetic limitations in antigen−antibody interactions, leading to a slightly lower-than-expected signal response. The LOD of the OV antigen in the urine sample is 1.68 ng mL$^{-1}$. The interferences from urine proteins were observed to be minimal even when the undiluted urine was applied. The resulting LOD and dynamic range in urine


https://doi.org/10.1021/acsomega.5c00633
ACS Omega 2025, 10, 13621−13633

measurement represent real-world diagnostic conditions where matrix effects are unavoidable. The application of the developed immunosensor to the real clinical sample supported its significance for the clinical diagnosis of OV infection.

Table 2 shows the LODs and linear ranges of various other detection methods for OV antigens compared to our study.

**Table 2. Comparison of the LODs and Linearity of Various Detection Methods for the OV Antigen**

| methods | limit of detection | linearity | reference |
|---|---|---|---|
| OV excretory-secretory (OV-ES) ELISA | 39 ng $mL^{-1}$ | | 65 |
| AuNPs-ELISA assay | 23.9 ng $mL^{-1}$ | 5.9−12,000 ng $mL^{-1}$ | 69 |
| enzyme-linked immunosorbent assay | 93.8 ng $mL^{-1}$ | | 70 |
| smartphone-based fluorescent ELISA | 34 ng $mL^{-1}$ | 1.95−125 ng $mL^{-1}$ | 71 |
| OV rapid test kit | 28.5 ng $mL^{-1}$ | 28.5−5000 ng $mL^{-1}$ | 66 |
| electrochemical immunosensor | 0.08 ng $mL^{-1}$ | 0.2−200 $\mu$g $mL^{-1}$ | 21 |
| GO-Nf-mAb bioconjugate-based electrochemical sensor | 1.68 ng $mL^{-1}$ | 0.16−100 $\mu$g $mL^{-1}$ | this study |

The proposed electrochemical immunosensor exhibited a relatively low LOD with a greater detection range and high sensitivity. Superior to our previous innovation, the new bioconjugate exhibited a blocking-free and simpler fabrication process as well as increased stability of the GO-mAb conjugate, indicating that it can detect OV antigens across a wide concentration spectrum with higher sensitivity. Our approach using Nafion as a copolymer to enhance the bioconjugation of GO and mAb was successfully implemented and shows promise for electrochemical biosensing of the OV antigen. However, the cross-reactivity with other liver fluke parasites is yet to be disclosed for the developed biosensor. The detection limit of our GO-Nf-mAb biosensor (1.68 ng $mL^{-1}$) falls well below the established threshold for OV-negative cases (<32.9 ng $mL^{-1}$), suggesting strong potential for early-stage detection. According to the OV rapid detection test and ELISA grading scores, OV-negative cases are defined as <32.9 ng $mL^{-1}$, low infection as <80.0 ng $mL^{-1}$, moderate infection as <200 ng $mL^{-1}$, and high infection as >200 ng $mL^{-1}$.[66] Our biosensor demonstrates a detection range of 0.16−100 $\mu$g $mL^{-1}$, which encompasses the clinically relevant range for all stages of OV infection. Previous studies have demonstrated that urinary OV antigen levels correlated significantly with OV infection intensity.[65,67] The high sensitivity of our biosensor, particularly at low concentrations, indicates its potential utility for diagnosing early-stage infection, screening, treatment monitoring, and reinfection assessment for opisthorchiasis.[68] To further confirm the clinical usefulness and diagnostic efficacy of the immunosensor, a correlation study between the intensity of OV eggs as determined by the gold standard fecal examination procedures and the concentration of the OV antigen in urine as detected by the immunosensor should be carried out in the future to implement the developed electrochemical biosensor in point-of-care monitoring of OV infection.

**2.8. Reproducibility and Repeatability of the Immunosensor.** The repeatability and reproducibility of the proposed immunosensor were evaluated by analyzing the OV antigen (2 $\mu$g $mL^{-1}$) over 10 independent tests, with measurements taken both within a single run and across different runs performed by various operators. The relative standard deviations (RSD) obtained for reproducibility and repeatability were 9.65 and 6.47%, respectively. Therefore, the data indicated that the immunosensor could generate highly reproducible signals alongside highly consistent electrode surface modifications and precision.

## 3. CONCLUSIONS

A novel GO-Nf-mAb conjugate was synthesized for the sensitive detection of OV antigens. Using advanced techniques, including NEXAFS and XPS, the impact of Nafion on GO stability and antibody conjugation is thoroughly examined, providing in-depth molecular-level insights. Our research effectively illustrated the considerable benefits of using Nafion as an ionic copolymer to enhance the GO conjugation process with monoclonal antibodies, which solved the problems of GO self-aggregation and poor antibody immobilization seen in earlier investigations. We developed an innovative electrochemical immunosensor using this all-in-one bioconjugate, which functions as a bioreceptor, transducer, and blocking reagent simultaneously. The resulting electrochemical immunosensor exhibited a low detection limit in spiked urine (1.68 ng $mL^{-1}$), broad linearity, and a facilitated fabrication process. Our findings indicate that Nafion enhances antibody immobilization on the GO surface while preserving GO's activity, ultimately improving assay sensitivity. However, for potential clinical applications, further investigations into Nafion's biocompatibility and possible immunogenic effects would be valuable to ensure its safety in long-term use. Although the GO-Nf-mAb bioconjugate has shown potential for OV detection, the correct orientation of antibodies for specific antigen binding and the impact of Nafion on monoclonal antibodies to enhance the bioconjugation process remain unclear. Further studies will be conducted to assess the analytical performance of the bioconjugate-based immunosensor, with a focus on the sensor's stability and clinical applicability. In conclusion, this study demonstrated the GO-Nf-mAb conjugate's improved functional, structural, and electrochemical characteristics over the Nafion-free conjugate, underscoring the unexploited promise of Nafion in bioconjugation applications. These findings provide a strategy for achieving more effective bioconjugation for electrochemical biosensing applications, bringing up new possibilities for the application of Nafion in biosensor development.

## 4. MATERIALS AND METHODS

**4.1. Materials.** The crude somatic antigen of *Opisthorchis viverrini* and a monoclonal antibody specific to the OV somatic antigen (mAb, KKU 505) were prepared by one of the coauthors (PS). Graphene oxide (GO), Nafion 117 solution (5%), *N*-(3-(dimethylamino)propyl)-*N*-ethylcarbodiimide hydrochloride (EDC), *N*-hydroxysuccinimide (NHS), 4-morpholinoethanesulfonic acid (MES) free acid, and bovine serum albumin (BSA) were obtained from Sigma-Aldrich (Singapore). Potassium ferricyanide ($K_3[Fe(CN)_6]$, 5 mM) with 0.1 M potassium chloride (KCl) in phosphate-buffered saline (PBS) (1×, pH 7.4) was used as a redox indicator. Washing buffer (1× PBS, pH 7.4) was used between each coating procedure.



https://doi.org/10.1021/acsomega.5c00633
ACS Omega 2025, 10, 13621−13633

An AZ P4620 photoresist and an AZ 400 K developer were obtained from Merck Performance Materials GmBH (Germany). Gold and chromium pellets (Kurt J. Lesker Company, USA) were used for substrate preparation. Krohn silver electroplating solution (Krohn Industries, Inc., New Jersey) was applied for electroplating. Potassium iodide:iodide:hydrogen peroxide (10 g:2.5 g:100 mL) was used for Au etching, and 50% HCl was used as a chromium etchant. Microelectrode fabrication was performed in the Microsystems, Electronics, and Control System Laboratory (MECS), at the Synchrotron Light Research Institute (Nakhon Ratchasima, Thailand).

**4.2. Instruments and Characterization.** The voltammograms were obtained on a PalmSens4 potentiostat (PalmSens BV Co., Ltd., The Netherlands) with PS Trace 5.9 software. CV was performed by applying a potential of −0.5 to 0.5 V at a scan rate of 100 mV $s^{-1}$, and EIS was measured in the frequency range of 100 MHz to 100 kHz in 0.01 M PBS containing 5 mM $[Fe(CN)_6]^{3-/4-}$ and 0.1 M KCl. DPV measurements were performed in the potential range of −0.4 to 0.5 V with a step potential of 5 mV, a pulse potential of 70 mV, and a scan rate of 16 mV $s^{-1}$. The characterization of the prepared bioconjugates was performed via an atomic force microscope (AFM, Park systems, NX-10, Korea), a field-emission scanning electron microscope (FE-SEM, Jeol, JSM-IT200 InTouchScope, Tokyo, Japan), an FE-SEM-energy dispersive spectrometer (EDS) (Jeol, JSM-7800F, Tokyo, Japan), a Bruker TENSOR II attenuated total reflectance (ATR)-Fourier transform infrared (FTIR) spectrometer (Bruker, Germany), an XploRA plus Raman spectrometer (Horiba, Kyoto, Japan), and a Zetasizer Nano ZS (Malvern, England).

**4.3. Fabrication of Biosensing Electrodes.** The glass substrates (2.5 × 2.5 cm) were first thoroughly cleaned in fuming $NH_3$:$H_2O_2$ solution for 15 min and subsequently rinsed in running deionized (DI) water for 10 min. The clean glass slides were dried with nitrogen air and incubated in a hot-air oven at 120 °C for 10 min. The biosensing chip involved a three-electrode system with working and counter Au electrodes and a silver/silver chloride (Ag/AgCl) reference electrode. A thin layer of 200 nm Au was deposited on a glass substrate via the E-beam evaporation technique. A 20 nm chromium film was deposited in situ prior to Au deposition to facilitate adhesion between the Au layer and the glass substrate. The detailed deposition parameters for Cr and Au film growth are listed in Table S1. The patterning of the Au electrodes was performed via conventional photolithography via a photoresist (AZ P4620). The positive photoresist was spin-coated on the Au-deposited glass substrate (step at 1−500 rpm for 10 s and step at 2−4500 rpm for 30 s) to obtain a 3 μm-thick layer. Afterward, the spin-coated resist was prebaked at 95 °C for 3 min, exposed to UV irradiation (exposure at 825 mJ/$cm^2$), and developed in an AZ developer for 1 min. The developed photoresist was rinsed in demineralized water before hard baking (95 °C for 15 min) on a hot plate. The Au substrate was etched off with Au and Cr etchants, leaving the desired electrode areas, followed by the removal of photoresists by acetone. The second photoresist coating was performed by using a higher spin speed of 5500 rpm for 30 s to obtain a lower thickness of 1.5 μm. The thickness of the photoresists was confirmed via a 3D optical profilometer. The patterning of the reference electrode was performed via the same photolithography procedure as mentioned above, except that the negative photomask was applied instead. For the fabrication of the Ag/AgCl reference electrode, the commercial silver electroplating solution was filled in an electrochemical cell with a platinum wire in the reservoir and served as a counter electrode in the reference channel at 1.5 mA for 2 min. Subsequently, the silver electroplating solution was replaced with 0.1 M HCl solution, and then, the electroplated silver layer was electrochemically oxidized to form a AgCl layer at 1.5 mA for 2 min. The resist was then removed by the lift-off process.

**4.4. Preparation of the GO-Nf Nanocomposite and GO-Nf-mAb Bioconjugate.** The functionalization of GO was performed by suspending the GO powder (0.05 g) in 10 mL of MES buffer (0.1 M, pH 5.5) containing 100 μM EDC and 100 μM NHS. The suspension was stirred for 4 h at RT, centrifuged, and washed twice with PBS at 16,100*g* for 25 min to remove excess EDC and NHS attached. The supernatant was discarded, and the remaining pellets were solidified at 60 °C overnight. Activated GO (1 mg $mL^{-1}$) was resuspended in DI water by magnetic stirring for 30 min at room temperature followed by sonication for 10 min. A 5% Nafion solution was added to the GO suspension (1 mg $mL^{-1}$) and stirred for 24 h. The GO-Nf nanocomposite was further ultrasonicated for 15 min to obtain a uniform suspension.

Next, 20 μL of the monoclonal OV antibody was added to the GO-Nf solution (200 μL) and conjugated at RT for 1.5 h. BSA (10 μL, 0.5%) was added to the conjugate to block unbound GO-Nf surfaces in the solution. The conjugate was then centrifuged at 16,100*g* for 15 min and washed twice with PBS to remove excess BSA. The resulting GO-Nf-mAb conjugate was stored at 4 °C for further immobilization on the electrode sensor.

**4.5. X-ray Photoelectron Spectroscopy (XPS) Measurements.** XPS analysis was performed at the SUT-NANOTEC-SLRI joint research facility at the Synchrotron Light Research Institute (SLRI), Nakhon Ratchasima, Thailand. The samples were mounted on the stainless plate sample holder before being transferred into the vacuum chamber, where the base pressure was controlled at $4 \times 1 \times 10^{-9}$ mbar. A scanning XPS microprobe (PHI5000 VersaProbe II, ULVAC-PHI) was operated via X-rays from aluminum K$\alpha$ radiation at 1486.6 eV and was monochromatized and focused on the sample surface at a size of 100 μm by a quartz crystal. The XPS spectra for C 1s, N 1s, O 1s, and F 1s were measured at binding energy ranges of 275−300, 385−410, 520−545, and 680−695 eV, respectively, at a step size of 0.1 eV.

**4.6. Synchrotron Radiation-Based Near-Edge X-ray Absorption Fine Structure Spectroscopy (NEXAFS).** The NEXAFS measurement was also performed at the end station of BL3.2a. The beamline photon source covers an energy range of 40−1040 eV at a resolving power of 10,000. The NEXAFS spectra were measured in total electron yield mode at an incident angle of 60°, and the light polarization was parallel to the surface (s-polarization) at any light incident angle; that is, there was no influence of X-ray polarization. The $I_e$ (electron yield current) was calculated by the equation $I_e = I_0 \mu L$, where $L$ is the sampling depth. The total energy resolution was ∼0.5 eV. The C−K edge and O−K edge NEXAFS spectra were measured in the energy ranges of 280−320 and 515−550 eV at an energy step of 0.1 eV, respectively. In this study, the relative $sp^2$ content was evaluated based on the $\pi^*$ peak of the C−K edge spectra, following procedures described in the literature.[72,73]



https://doi.org/10.1021/acsomega.5c00633
ACS Omega 2025, 10, 13621−13633

**Scheme 1. Overall Representation of Bioconjugate-Based Electrochemical Immunosensor Representing (a) All-in-One GO-Nf-mAb Bioconjugate Preparation, (b) Dropcoating on the Au Electrode Surface, (c) Sample Incubation, and (d) Electrochemical Measurement**

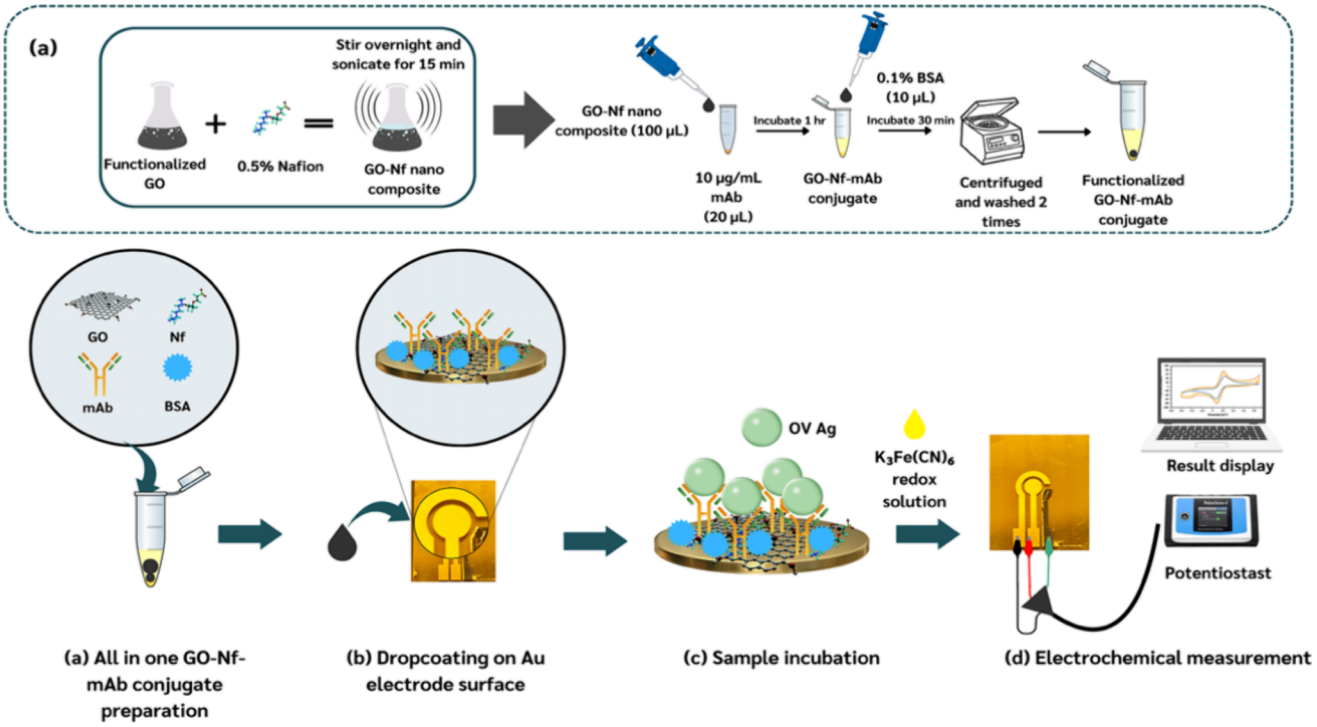


**4.7. Immunosensor Fabrication.** The immunosensor was constructed simply by dropcoating the GO-Nf-mAb conjugate on the working electrode (WE) surface. The bioconjugate was immobilized on the Au surface by physical adsorption, and the blocking step was omitted as an all-in-one conjugate was applied. To prevent the nonspecific adsorption of monoclonal antibodies on the electrode surface, the entire electrode surface was uniformly coated with the bioconjugate. Seven microliters of GO-Nf-mAb was incubated on the WE for 90 min and then washed with PBS. CV, EIS, and DPV measurements were performed for characterization and detection. The peak current obtained was denoted as $I_0$ as a baseline measurement for OV sensor calibration.

**4.8. Electrochemical Measurements.** Different concentrations of somatic OV antigens were incubated with the prepared immunosensor for 60 min. After the sample was rinsed with PBS, 150 $\mu$L of 5 mM $[Fe(CN)_6]^{3-/4-}$ was added until all the electrode surfaces were submerged. The detection of the OV antigen was measured with DPV. A schematic diagram of the overall fabrication of the microfluidics device and the electrochemical measurements is shown in Scheme 1. The peak currents before ($I_0$) and after ($I_1$) OV antigen detection were recorded. The peak current changes ($\Delta I = I_0 - I_1$) were observed to correlate with the OV antigen concentration present in the sample.

## ■ ASSOCIATED CONTENT

### Data Availability Statement

Data sharing is not applicable.

### Supporting Information

The Supporting Information is available free of charge at https://pubs.acs.org/doi/10.1021/acsomega.5c00633.

(Table S1) E-beam evaporation parameters for Cr and Au deposition; (Figure S1) stability of GO and GO-Nf dispersion in aqueous solution and electrochemical stability for 7 days; (Figure S2) fabrication of the Ag/AgCl reference electrode; (Figure S3) FE-SEM images; (Table S2) atomic percentages of carbon, nitrogen, oxygen, and fluorine; (Table S3) XPS compositional analysis, functional groups, and binding energies representing C 1s, N 1s, O 1s, and F 1s spectra; methods for production of monoclonal Ab and crude somatic OV antigen extraction (PDF)

## ■ AUTHOR INFORMATION


### Corresponding Author

**Jureerut Daduang** − *Centre for Research and Development of Medical Diagnostic Laboratories, Faculty of Associated Medical Sciences, Khon Kaen University, Khon Kaen 40002, Thailand;* orcid.org/0009-0009-5088-811X; Email: jurpoo@kku.ac.th

### Authors

**Nang Noon Shean Aye** − *Biomedical Sciences Program, Graduate School and Centre for Research and Development of Medical Diagnostic Laboratories, Faculty of Associated Medical Sciences, Khon Kaen University, Khon Kaen 40002, Thailand*

**Pornsuda Maraming** − *Centre for Research and Development of Medical Diagnostic Laboratories, Faculty of Associated Medical Sciences, Khon Kaen University, Khon Kaen 40002, Thailand*

**Patcharaporn Tippayawat** − *Centre for Research and Development of Medical Diagnostic Laboratories, Faculty of*




https://doi.org/10.1021/acsomega.5c00633
ACS Omega 2025, 10, 13621−13633

*Associated Medical Sciences, Khon Kaen University, Khon Kaen 40002, Thailand;* orcid.org/0000-0002-4452-1284
**Sakda Daduang** − *Division of Pharmacognosy and Toxicology, Faculty of Pharmaceutical Sciences, Khon Kaen University, Khon Kaen 40002, Thailand*
**Anchalee Techasen** − *Centre for Research and Development of Medical Diagnostic Laboratories, Faculty of Associated Medical Sciences and Cholangiocarcinoma Research Institute, Khon Kaen University, Khon Kaen 40002, Thailand*
**Paiboon Sithithaworn** − *Cholangiocarcinoma Research Institute and Department of Parasitology, Faculty of Medicine, Khon Kaen University, Khon Kaen 40002, Thailand*
**Roengrut Rujanakraikarn** − *Synchrotron Light Research Institute (Public Organization), Nakhon Ratchasima 30000, Thailand*
**Nichada Jearanaikoon** − *Synchrotron Light Research Institute (Public Organization), Nakhon Ratchasima 30000, Thailand*
**Rungrueang Phatthanakun** − *Synchrotron Light Research Institute (Public Organization), Nakhon Ratchasima 30000, Thailand*
**Ratchadaporn Supruangnet** − *Synchrotron Light Research Institute (Public Organization), Nakhon Ratchasima 30000, Thailand*
**Pat Photongkam** − *Synchrotron Light Research Institute (Public Organization), Nakhon Ratchasima 30000, Thailand;* orcid.org/0000-0002-0645-2126

Complete contact information is available at: https://pubs.acs.org/10.1021/acsomega.5c00633

### Author Contributions

Conceptualization, N.N.S.A., P.M., and J.D.; formal analysis, N.N.S.A.; investigation, N.N.S.A.; methodologies, N.N.S.A. and N.J.; supervision, P.M., N.J., R.P., and J.D.; writing of the original draft, N.N.S.A.; review and editing, N.N.S.A., S.D., P.T., A.T., P.M., P.S., N.J., R.P., and J.D.; resources, P.S.

### Funding

This research was supported by the Fundamental Fund of Khon Kaen University and the National Science, Research, and Innovation Fund (NSRF) (Year 2023), the Basic Research Fund of Khon Kaen University through the Cholangiocarcinoma Research Institute CARI-BRF64-47, and a Khon Kaen University ASEAN-GMS scholarship. This study was also supported by the Centre of Research and Development of Medical Diagnostic Laboratories (CMDL), Faculty of Associated Medical Sciences, Khon Kaen University.

### Notes

The authors declare no competing financial interest.
The study was conducted in accordance with the Declaration of Helsinki, and the protocol was approved by the Centre for Ethics in Human Research, Khon Kaen University (HE664025).
Informed consent was obtained from all the subjects involved in the study.

## ■ ACKNOWLEDGMENTS

The authors would like to express gratitude for a Khon Kaen University ASEAN-GMS scholarship. The authors acknowledge Dr. Ratchadaporn Supruangnet (BL 3.2, SLRI) for support and assistance with the NEXAFS measurements and Dr. Pat Phothongkum (SUT-NANOTEC-SLRI research facility) for support with the XPS measurements. Microfabrication of the electrodes was performed at Microsystems, Electronics, and Control System Laboratory (MECS), at Synchrotron Light Research Institute (Nakhon Ratchasima, Thailand).

## ■ REFERENCES

(1) Cancelliere, R.; Di Tinno, A.; Cataldo, A.; Bellucci, S.; Kumbhat, S.; Micheli, L. Nafion-Based Label-Free Immunosensor as a Reliable Warning System: The Case of AFB1 Detection in Cattle Feed. *Microchem. J.* **2023**, *191*, No. 108868.
(2) Mohamad, N. R.; Marzuki, N. H. C.; Buang, N. A.; Huyop, F.; Wahab, R. A. An Overview of Technologies for Immobilization of Enzymes and Surface Analysis Techniques for Immobilized Enzymes. *Biotechnol. Biotechnol. Equip.* **2015**, *29* (2), 205−220.
(3) Rana, S.; Shaw, R.; Kumar, R.; Chakraborty, P.; Bandyopadhyay, S.Chapter Two - Bioconjugates: Preparation Methods and Therapeutic Applications. In *Comprehensive Analytical Chemistry*; Verma, S. K.; Das, A. K., Eds.; Bioconjugated Materials Part 1 Preparation, Characterization and Applications in Therapeutics, Environmental monitoring and Point-of-care diagnostics; Elsevier: 2023; Vol. *102*, pp 43−91. .
(4) Putzbach, W.; Ronkainen, N. J. Immobilization Techniques in the Fabrication of Nanomaterial-Based Electrochemical Biosensors: A Review. *Sensors* **2013**, *13* (4), 4811−4840.
(5) Nurunnabi, M.; Parvez, K.; Nafiujjaman, M.; Revuri, V.; Khan, H. A.; Feng, X.; Lee, Y. Bioapplication of Graphene Oxide Derivatives: Drug/Gene Delivery, Imaging, Polymeric Modification, Toxicology, Therapeutics and Challenges. *RSC Adv.* **2015**, *5* (52), 42141−42161.
(6) Sharma, D.; Kanchi, S.; Sabela, M. I.; Bisetty, K. Insight into the Biosensing of Graphene Oxide: Present and Future Prospects. *Arab. J. Chem.* **2016**, *9* (2), 238−261.
(7) Bertoncello, P.; Ram, M. K.; Notargiacomo, A.; Ugo, P.; Nicolini, C. Fabrication and Physico-Chemical Properties of Nafion Langmuir−Schaefer Films. *Phys. Chem. Chem. Phys.* **2002**, *4* (16), 4036−4043.
(8) Tsai, Y.-C.; Li, S.-C.; Chen, J.-M. Cast Thin Film Biosensor Design Based on a Nafion Backbone, a Multiwalled Carbon Nanotube Conduit, and a Glucose Oxidase Function. *Langmuir* **2005**, *21* (8), 3653−3658.
(9) Yusoff, N. Chapter 7 - Graphene−Polymer Modified Electrochemical Sensors. In *Graphene-Based Electrochemical Sensors for Biomolecules*; Pandikumar, A.; Rameshkumar, P., Eds.; Micro and Nano Technologies; Elsevier, 2019; pp 155−186. .
(10) Er, E.; Çelikkan, H.; Erk, N.; Aksu, M. L. A New Generation Electrochemical Sensor Based on Graphene Nanosheets/Gold Nanoparticles/Nafion Nanocomposite for Determination of Silodosin. *Electrochim. Acta* **2015**, *157*, 252−257.
(11) Brownson, D. A. C.; Banks, C. E. Graphene Electrochemistry: Fabricating Amperometric Biosensors. *Analyst* **2011**, *136* (10), 2084−2089.
(12) Sanghavi, B. J.; Kalambate, P. K.; Karna, S. P.; Srivastava, A. K. Voltammetric Determination of Sumatriptan Based on a Graphene/Gold Nanoparticles/Nafion Composite Modified Glassy Carbon Electrode. *Talanta* **2014**, *120*, 1−9.
(13) Muniandy, S.; Thong, K. L.; Appaturi, J. N.; Lai, C. W.; Leo, B. F. Electrochemical Aptasensor for Salmonella Detection Using Nafion-Doped Reduced Graphene Oxide. *Sens. Diagn.* **2022**, *1* (6), 1209−1217.
(14) Ni, Y.; Wang, P.; Song, H.; Lin, X.; Kokot, S. Electrochemical Detection of Benzo(a)Pyrene and Related DNA Damage Using DNA/Hemin/Nafion−Graphene Biosensor. *Anal. Chim. Acta* **2014**, *821*, 34−40.
(15) Hlavatá, L.; Vyskočil, V.; Beníková, K.; Borbélyová, M.; Labuda, J. DNA-Based Biosensors with External Nafion and Chitosan Membranes for the Evaluation of the Antioxidant Activity of Beer, Coffee, and Tea. *Open Chem.* **2014**, *12* (5), 604−611.

(16) Zhou, Y.-M.; Wu, Z.-Y.; Shen, G.-L.; Yu, R.-Q. An Amperometric Immunosensor Based on Nafion-Modified Electrode for the Determination of *Schistosoma Japonicum* Antibody. *Sens. Actuators B Chem.* **2003**, *89* (3), 292−298.
(17) Andrews, R. H.; Sithithaworn, P.; Petney, T. N. Opisthorchis Viverrini: An Underestimated Parasite in World Health. *Trends Parasitol.* **2008**, *24* (11), 497−501.
(18) Sripa, B.; Bethony, J. M.; Sithithaworn, P.; Kaewkes, S.; Mairiang, E.; Loukas, A.; Mulvenna, J.; Laha, T.; Hotez, P. J.; Brindley, P. J. Opisthorchiasis and Opisthorchis-Associated Cholangiocarcinoma in Thailand and Laos. *Acta Trop.* **2011**, *120* (Suppl 1), S158−S168.
(19) Almanfaluthi, M.; Widodo, S.; Suttiprapa, S.; Wongsaroj, T.; Sripa, B. The Burden of Opisthorchiasis and Leptospirosis in Thailand: A Nationwide Syndemic Analysis. *Acta Trop.* **2022**, *226*, No. 106227.
(20) Sripa, B.; Tangkawattana, S.; Brindley, P. J. Update on Pathogenesis of Opisthorchiasis and Cholangiocarcinoma. *Adv. Parasitol.* **2018**, *102*, 97−113.
(21) Aye, N. N. S.; Maraming, P.; Tippayawat, P.; Daduang, S.; Techasen, A.; Jamnongkan, W.; Sithithaworn, P.; Daduang, J. Functionalized Graphene Oxide−Antibody Conjugate-Based Electrochemical Immunosensors to Detect Opisthorchis Viverrini Antigen in Urine. *Mater. Adv.* **2024**, *5*, 4491.
(22) Wang, Z.; Hao, Z.; Wang, X.; Huang, C.; Lin, Q.; Zhao, X.; Pan, Y. A Flexible and Regenerative Aptameric Graphene−Nafion Biosensor for Cytokine Storm Biomarker Monitoring in Undiluted Biofluids toward Wearable Applications. *Adv. Funct. Mater.* **2021**, *31* (4), No. 2005958.
(23) Lee, Y. J.; Kim, J. D.; Park, J. Y. Nafion Coated Enzyme Free Glucose Micro-Biosensors for Anti-Fouling of Protein. In *2009 4th IEEE International Conference on Nano/Micro Engineered and Molecular Systems*; IEEE: 2009; pp 335−338. .
(24) Jain, R.; Nirbhaya, V.; Chandra, R.; Kumar, S. Nanostructured Mesoporous Carbon Based Electrochemical Biosensor for Efficient Detection of Swine Flu. *Electroanalysis* **2022**, *34* (1), 43−55.
(25) Ohno, R.; Ohnuki, H.; Wang, H.; Yokoyama, T.; Endo, H.; Tsuya, D.; Izumi, M. Electrochemical Impedance Spectroscopy Biosensor with Interdigitated Electrode for Detection of Human Immunoglobulin A. *Biosens. Bioelectron.* **2013**, *40* (1), 422−426.
(26) Törer, H.; Aydın, E. B.; Sezgintürk, M. K. A Label-Free Electrochemical Biosensor for Direct Detection of RACK 1 by Using Disposable, Low-Cost and Reproducible ITO Based Electrode. *Anal. Chim. Acta* **2018**, *1024*, 65−72.
(27) Ghosh, K.; Kumar, M.; Maruyama, T.; Ando, Y. Tailoring the Field Emission Property of Nitrogen-Doped Carbon Nanotubes by Controlling the Graphitic/Pyridinic Substitution. *Carbon* **2010**, *48* (1), 191−200.
(28) Han, P.; Yue, Y.; Zhang, L.; Xu, H.; Liu, Z.; Zhang, K.; Zhang, C.; Dong, S.; Ma, W.; Cui, G. Nitrogen-Doping of Chemically Reduced Mesocarbon Microbead Oxide for the Improved Performance of Lithium Ion Batteries. *Carbon* **2012**, *50* (3), 1355−1362.
(29) Peng, K.-J.; Lai, J.-Y.; Liu, Y.-L. Nanohybrids of Graphene Oxide Chemically-Bonded with Nafion: Preparation and Application for Proton Exchange Membrane Fuel Cells. *J. Membr. Sci.* **2016**, *514*, 86−94.
(30) Jun, S. C. Fundamental of Graphene. In *Graphene-based Energy Devices*; John Wiley & Sons, Ltd: 2015; pp 1−48. .
(31) Sudesh; Kumar, N.; Das, S.; Bernhard, C.; Varma, G. D. Effect of Graphene Oxide Doping on Superconducting Properties of Bulk MgB2. *Supercond. Sci. Technol.* **2013**, *26* (9), No. 095008.
(32) Shan, C.; Yang, H.; Song, J.; Han, D.; Ivaska, A.; Niu, L. Direct Electrochemistry of Glucose Oxidase and Biosensing for Glucose Based on Graphene. *Anal. Chem.* **2009**, *81* (6), 2378−2382.
(33) Stankovich, S.; Piner, R. D.; Chen, X.; Wu, N.; Nguyen, S. T.; Ruoff, R. S. Stable Aqueous Dispersions of Graphitic Nanoplatelets via the Reduction of Exfoliated Graphite Oxide in the Presence of Poly(Sodium 4-Styrenesulfonate). *J. Mater. Chem.* **2006**, *16* (2), 155−158.
(34) Shan, C.; Yang, H.; Han, D.; Zhang, Q.; Ivaska, A.; Niu, L. Water-Soluble Graphene Covalently Functionalized by Biocompatible Poly-L-Lysine. *Langmuir* **2009**, *25* (20), 12030−12033.
(35) Tertiş, M.; Hosu, O.; Fritea, L.; Farcau, C.; Cernat, A.; Săndulescu, R.; Cristea, C. A Novel Label-Free Immunosensor Based on Activated Graphene Oxide for Acetaminophen Detection. *Electroanalysis* **2015**, *27* (3), 638−647.
(36) Hwang, T.; Palmre, V.; Nam, J.; Lee, D.-C.; Kim, K. J. A New Ionic Polymer−Metal Composite Based on Nafion/Poly(Vinyl Alcohol-Co-Ethylene) Blends. *Smart Mater. Struct.* **2015**, *24* (10), No. 105011.
(37) Kunimatsu, K.; Yoda, T.; Tryk, D. A.; Uchida, H.; Watanabe, M. In Situ ATR-FTIR Study of Oxygen Reduction at the Pt/Nafion Interface. *Phys. Chem. Chem. Phys.* **2010**, *12* (3), 621−629.
(38) Kumar, R.; Xu, C.; Scott, K. Graphite Oxide/Nafion Composite Membranes for Polymer Electrolyte Fuel Cells. *RSC Adv.* **2012**, *2* (23), 8777−8782.
(39) Laporta, M.; Pegoraro, M.; Zanderighi, L. Perfluorosulfonated Membrane (Nafion): FT-IR Study of the State of Water with Increasing Humidity. *Phys. Chem. Chem. Phys.* **1999**, *1* (19), 4619−4628.
(40) Sigwadi, R.; Mokrani, T.; Msomi, P.; Nemavhola, F. The Effect of Sulfated Zirconia and Zirconium Phosphate Nanocomposite Membranes on Fuel-Cell Efficiency. *Polymers* **2022**, *14* (2), 263.
(41) Di Noto, V.; Gliubizzi, R.; Negro, E.; Pace, G. Effect of SiO2 on Relaxation Phenomena and Mechanism of Ion Conductivity of [Nafion/(SiO2)x] Composite Membranes. *J. Phys. Chem. B* **2006**, *110* (49), 24972−24986.
(42) Yumitori, S. Correlation of C1s Chemical State Intensities with the O1s Intensity in the XPS Analysis of Anodically Oxidized Glass-like Carbon Samples. *J. Mater. Sci.* **2000**, *35* (1), 139−146.
(43) Rani, J. R.; Lim, J.; Oh, J.; Kim, D.; Lee, D.; Kim, J.-W.; Shin, H. S.; Kim, J. H.; Jun, S. C. Substrate and Buffer Layer Effect on the Structural and Optical Properties of Graphene Oxide Thin Films. *RSC Adv.* **2013**, *3* (17), 5926−5936.
(44) Johra, F. T.; Lee, J.-W.; Jung, W.-G. Facile and Safe Graphene Preparation on Solution Based Platform. *J. Ind. Eng. Chem.* **2014**, *20* (5), 2883−2887.
(45) Ihalainen, P.; Majumdar, H.; Viitala, T.; Törngren, B.; Närjeoja, T.; Määttänen, A.; Sarfraz, J.; Härmä, H.; Yliperttula, M.; Österbacka, R.; Peltonen, J. Application of Paper-Supported Printed Gold Electrodes for Impedimetric Immunosensor Development. *Biosensors* **2013**, *3* (1), 1−17.
(46) Ravi, S.; Zhang, S.; Lee, Y.-R.; Kang, K.-K.; Kim, J.-M.; Ahn, J.-W.; Ahn, W.-S. EDTA-Functionalized KCC-1 and KIT-6 Mesoporous Silicas for Nd3+ Ion Recovery from Aqueous Solutions. *J. Ind. Eng. Chem.* **2018**, *67*, 210−218.
(47) Barazzouk, S.; Daneault, C. Amino Acid and Peptide Immobilization on Oxidized Nanocellulose: Spectroscopic Characterization. *Nanomaterials* **2012**, *2* (2), 187−205.
(48) Kamra, T.; Chaudhary, S.; Xu, C.; Montelius, L.; Schnadt, J.; Ye, L. Covalent Immobilization of Molecularly Imprinted Polymer Nanoparticles on a Gold Surface Using Carbodiimide Coupling for Chemical Sensing. *J. Colloid Interface Sci.* **2016**, *461*, 1−8.
(49) Lai, L.-J.; Yang, Y.-W.; Lin, Y.-K.; Huang, L.-L.; Hsieh, Y.-H. Surface Characterization of Immunosensor Conjugated with Gold Nanoparticles Based on Cyclic Voltammetry and X-Ray Photoelectron Spectroscopy. *Colloids Surf. B Biointerfaces* **2009**, *68* (2), 130−135.
(50) Friedman, A. K.; Shi, W.; Losovyj, Y.; Siedle, A. R.; Baker, L. A. Mapping Microscale Chemical Heterogeneity in Nafion Membranes with X-Ray Photoelectron Spectroscopy. *J. Electrochem. Soc.* **2018**, *165* (11), H733.
(51) Kim, J.; Zhou, R.; Murakoshi, K.; Yasuda, S. Advantage of Semi-Ionic Bonding in Fluorine-Doped Carbon Materials for the Oxygen Evolution Reaction in Alkaline Media. *RSC Adv.* **2018**, *8* (26), 14152−14156.
(52) Martínez de Yuso, M. V.; Calderón, A. B.; Romero, V.; Cuberes, M. T.; Benavente, J. Chemical and Homogeneity Changes of


https://doi.org/10.1021/acsomega.5c00633
*ACS Omega* 2025, 10, 13621−13633

a Nafion Membrane Surface Associated to Its Doping with the Cation of the Room-Temperature Ionic Liquid AliquatCl. *Surf. Interface Anal.* **2016**, *48* (7), 561−565.
(53) Li, L.; Tian, X.; Meng, D.; Collins, M.; Wang, J.; Patterson, R.; Nguyen, L.; Yi, X. Processing, Characterization, and Impact of Nafion Thin Film on Photonic Nanowaveguides for Humidity Sensing. *Adv. Photonics Res.* **2022**, *3* (2), No. 2100181.
(54) Schultz, B. J.; Dennis, R. V.; Aldinger, J. P.; Jaye, C.; Wang, X.; Fischer, D. A.; Cartwright, A. N.; Banerjee, S. X-Ray Absorption Spectroscopy Studies of Electronic Structure Recovery and Nitrogen Local Structure upon Thermal Reduction of Graphene Oxide in an Ammonia Environment. *RSC Adv.* **2014**, *4* (2), 634−644.
(55) Ehlert, C.; Unger, W. E. S.; Saalfrank, P. C K-Edge NEXAFS Spectra of Graphene with Physical and Chemical Defects: A Study Based on Density Functional Theory. *Phys. Chem. Chem. Phys.* **2014**, *16* (27), 14083−14095.
(56) Gandhiraman, R. P.; Nordlund, D.; Javier, C.; Koehne, J. E.; Chen, B.; Meyyappan, M. X-Ray Absorption Study of Graphene Oxide and Transition Metal Oxide Nanocomposites. *J. Phys. Chem. C* **2014**, *118* (32), 18706−18712.
(57) Rabchinskii, M. K.; Besedina, N. A.; Brzhezinskaya, M.; Stolyarova, D. Y.; Ryzhkov, S. A.; Saveliev, S. D.; Antonov, G. A.; Baidakova, M. V.; Pavlov, S. I.; Kirilenko, D. A.; Shvidchenko, A. V.; Cherviakova, P. D.; Brunkov, P. N. Graphene Amination towards Its Grafting by Antibodies for Biosensing Applications. *Nanomaterials* **2023**, *13* (11), 1730.
(58) Nickl, P.; Radnik, J.; Azab, W.; Donskyi, I. S. Surface Characterization of Covalently Functionalized Carbon-Based Nanomaterials Using Comprehensive XP and NEXAFS Spectroscopies. *Appl. Surf. Sci.* **2023**, *613*, No. 155953.
(59) Wong, A.; Silva, T. A.; Vicentini, F. C.; Fatibello-Filho, O. Electrochemical Sensor Based on Graphene Oxide and Ionic Liquid for Ofloxacin Determination at Nanomolar Levels. *Talanta* **2016**, *161*, 333−341.
(60) He, C.; Wang, J.; Gao, N.; He, H.; Zou, K.; Ma, M.; Zhou, Y.; Cai, Z.; Chang, G.; He, Y. A Gold Electrode Modified with a Gold-Graphene Oxide Nanocomposite for Non-Enzymatic Sensing of Glucose at near-Neutral pH Values. *Microchim. Acta* **2019**, *186* (11), 722.
(61) Alam, A. U.; Deen, M. J. Bisphenol A Electrochemical Sensor Using Graphene Oxide and β-Cyclodextrin-Functionalized Multi-Walled Carbon Nanotubes. *Anal. Chem.* **2020**, *92* (7), 5532−5539.
(62) Chen, D.; Feng, H.; Li, J. Graphene Oxide: Preparation, Functionalization, and Electrochemical Applications. *Chem. Rev.* **2012**, *112* (11), 6027−6053.
(63) Azimzadeh, M.; Nasirizadeh, N.; Rahaie, M.; Naderi-Manesh, H. Early Detection of Alzheimer's Disease Using a Biosensor Based on Electrochemically-Reduced Graphene Oxide and Gold Nanowires for the Quantification of Serum microRNA-137. *RSC Adv.* **2017**, *7* (88), 55709−55719.
(64) García-González, R.; Fernández-Abedul, M. T.; Costa-García, A. Nafion® Modified-Screen Printed Gold Electrodes and Their Carbon Nanostructuration for Electrochemical Sensors Applications. *Talanta* **2013**, *107*, 376−381.
(65) Worasith, C.; Kamamia, C.; Yakovleva, A.; Duenngai, K.; Wangboon, C.; Sithithaworn, J.; Watwiengkam, N.; Namwat, N.; Techasen, A.; Loilome, W.; Yongvanit, P.; Loukas, A.; Sithithaworn, P.; Bethony, J. M. Advances in the Diagnosis of Human Opisthorchiasis: Development of Opisthorchis Viverrini Antigen Detection in Urine. *PLoS Negl. Trop. Dis.* **2015**, *9* (10), No. e0004157.
(66) Worasith, C.; Sithithaworn, J.; Wongphutorn, P.; Homwong, C.; Khongsukwiwat, K.; Techasen, A.; Kopolrat, K. Y.; Loilome, W.; Namwat, N.; Thinkamrop, B.; Tawarungruang, C.; Titapun, A.; Laha, T.; Andrews, R. H.; Taylor-Robinson, S. D.; Sithithaworn, P. Accuracy of a New Rapid Diagnostic Test for Urinary Antigen Detection and Assessment of Drug Treatment in Opisthorchiasis. *Infect. Dis. Poverty* **2023**, *12* (1), 102.
(67) Watwiengkam, N.; Sithithaworn, J.; Duenngai, K.; Sripa, B.; Laha, T.; Johansen, M. V.; Sithithaworn, P. Improved Performance and Quantitative Detection of Copro-Antigens by a Monoclonal Antibody Based ELISA to Diagnose Human Opisthorchiasis. *Acta Trop.* **2013**, *128* (3), 659−665.
(68) Worasith, C.; Wangboon, C.; Kopolrat, K. Y.; Homwong, C.; Sithithaworn, J.; Techasen, A.; Thanan, R.; Khuntikeo, N.; Sithithaworn, P. Application of Urine Antigen Assay to Evaluate Outcomes of Praziquantel Treatment and Reinfection in Opisthorchiasis in Northeast Thailand. *Trans. R. Soc. Trop. Med. Hyg.* **2020**, *114* (10), 751−761.
(69) Taron, W.; Jamnongkan, W.; Techasen, A.; Phetcharaburanin, J.; Namwat, N.; Sithithaworn, P.; Khuntikeo, N.; Mukdasai, S.; Sayasone, S.; Loilome, W.; Ngeontae, W. AuNPs-LISA, an Efficient Detection Assay for Opisthorchis Viverrini (Ov) Antigen in Urine. *Talanta* **2020**, *209*, No. 120592.
(70) Sirisinha, S.; Chawengkirttikul, R.; Haswell-Elkins, M. R.; Elkins, D. B.; Kaewkes, S.; Sithithaworn, P. Evaluation of a Monoclonal Antibody-Based Enzyme-Linked Immunosorbent Assay for the Diagnosis of Opisthorchis Viverrini Infection in an Endemic Area. *Am. J. Trop. Med. Hyg.* **1995**, *52* (6), 521−524.
(71) Taron, W.; Phooplub, K.; Sanchimplee, S.; Piyanamvanich, K.; Jamnongkan, W.; Techasen, A.; Phetcharaburanin, J.; Klanrit, P.; Namwat, N.; Khuntikeo, N.; Boonmars, T.; Sithithaworn, P.; Ouiganon, S.; Kanatharana, P.; Thavarungkul, P.; Buranachai, C.; Loilome, W.; Ngeontae, W. Smartphone-Based Fluorescent ELISA with Simple Fluorescent Enhancement Strategy for Opisthorchis Viverrini (Ov) Antigen Detection in Urine Samples. *Sens. Actuators B Chem.* **2021**, *348*, No. 130705.
(72) Outka, D. A.; Stöhr, J. Curve Fitting Analysis of Near-edge Core Excitation Spectra of Free, Adsorbed, and Polymeric Molecules. *J. Chem. Phys.* **1988**, *88* (6), 3539−3554.
(73) Mangolini, F.; McClimon, J. B.; Rose, F.; Carpick, R. W. Accounting for Nanometer-Thick Adventitious Carbon Contamination in X-Ray Absorption Spectra of Carbon-Based Materials. *Anal. Chem.* **2014**, *86* (24), 12258−12265.


https://doi.org/10.1021/acsomega.5c00633
*ACS Omega* 2025, 10, 13621−13633